Materials Horizons

Heteroepitaxial growth of highly anisotropic Sb2Se3 films on GaAs

Journal:	*Materials Horizons*
Manuscript ID	MH-COM-02-2025-000225.R1
Article Type:	Communication
Date Submitted by the Author:	28-Apr-2025
Complete List of Authors:	Xiao, Kelly; Stanford University Tara, Virat; University of Washington Reddy, Pooja; Stanford University Meyer, Jarod; Stanford University Skipper, Alec; University of California Santa Barbara Chen, Rui; University of Washington, Electrical engineering Nordin, Leland; University of Central Florida Majumdar, Arka; University of Washington Mukherjee, Kunal; Stanford University,

New Concepts Statement

Heteroepitaxial growth of highly anisotropic Sb_2Se_3 films on GaAs

Anisotropic chalcogenides present coveted properties but often require an understanding of synthesis routes that preserve their anisotropic properties in non-bulk forms. Insights into substrate engineering or other growth techniques are valuable in marrying low-dimensional chalcogenides with conventional cubic substrate counterparts. **We demonstrate the concept of harnessing symmetry-breaking surface reconstructions to yield oriented growth of "quasi-1D" antimony selenide (Sb_2Se_3) on isotropic semiconductor templates.** To date, Sb_2Se_3 growth is relatively immature, which is a potential reason the intrinsic anisotropy of Sb_2Se_3 single crystal is rarely reported in previous works on thin films. In contrast, we present findings on large optical anisotropy in the near-infrared among all three orthogonal directions in oriented Sb_2Se_3 thin films grown on reconstructed GaAs templates. This work aims to highlight fundamental synthesis-structure-property links in Sb_2Se_3. We turn the spotlight on Sb_2Se_3 thin films as a material with accessible strong anisotropy, opening further investigation for photonics applications that require phase or polarization control.

Heteroepitaxial growth of highly anisotropic Sb_2Se_3 films on GaAs

Kelly Xiao[1], Virat Tara[2], Pooja D. Reddy[1], Jarod E. Meyer[1], Alec M. Skipper[3], Rui Chen[2], Leland J. Nordin[4,5], Arka Majumdar[2,6], and Kunal Mukherjee[1]*

[1] Department of Materials Science and Engineering, Stanford University, Stanford, CA 94305, USA

[2] Department of Electrical and Computer Engineering, University of Washington, Seattle, WA 98195, USA

[3] Institute for Energy Efficiency, University of California Santa Barbara, Santa Barbara, CA 93106, USA

[4] Department of Materials Science and Engineering, University of Centra Florida, Orlando, FL 32816, USA

[5] CREOL, The College of Optics and Photonics, University of Central Florida, Orlando, FL 32816, USA

[6] Department of Physics, University of Washington, Seattle, WA 98195, USA

*Corresponding Author: kunalm@stanford.edu

The epitaxial integration of anisotropic materials with mainstream cubic semiconductors opens new routes to advanced electronic and photonic devices with directional properties. In this work, we synthesize heteroepitaxial thin films of orthorhombic "quasi-1D" Sb_2Se_3 on cubic GaAs(001) using molecular beam epitaxy. Traditionally, the synthesis of anisotropic films with low symmetry materials is challenging due to multiple grain orientations that form. On a macroscopic scale, such a film tends towards isotropic properties, even if individual grains possess anisotropic responses. We achieve epitaxial Sb_2Se_3 grains on pristine homoepitaxial GaAs templates at low temperatures of 180–200 °C. With the Sb_2Se_3 1D axis aligned in-plane to GaAs [110] and the primary van der Waals direction lying out-of-plane, we find a birefringence of 0.2 between in-plane orthogonal directions and a giant out-of-plane birefringence greater than 1 at telecom wavelengths. Growth at higher temperatures up to 265 °C yields Sb_2Se_3 of an unusual in-plane rotated texture that further enhances the in-plane optical index anisotropy to 0.3.

1. Introduction

Sb_2Se_3 is a layered material in the V_2-VI_3 chalcogenide family (e.g. Sb_2Te_3, Bi_2Se_3, Bi_2Te_3). Rather than crystallizing in the 2D rhombohedral structure as the prototypical members do, Sb_2Se_3 adopts the lower symmetry *Pbnm* orthorhombic structure.[1,2] Orthorhombic Sb_2Se_3 is isostructural with stibnite, which exhibits covalently chained bonding along only a single "needle" or 1D axis to form parallel ribboned units. Along the other two crystallographic directions, the ribbons loosely pack into a van der Waals ensemble owing to steric effects imparted by the Sb $5s^2$ lone pair.[3] These asymmetric interactions along each primary axis in Sb_2Se_3 are the origin of its quasi-1D character. Unsurprisingly, a set of unique optoelectronic and structure-related properties converge in this low-dimensional system, among these favorable electronic and thermal transport along the needle axis,[4] as well as high absorption of the visible wavelengths (E_g = 1.1 – 1.2 eV).[5,6] In light of these compelling qualities, Sb_2Se_3 has been proposed as a candidate material for thermoelectric alloys[7,8] and photovoltaic absorbers.[9–14] The inherent 1D nanostructure of this material has additionally inspired a technological focus on its "benign grain boundaries", which in theory are intrinsically passivated and potentially self-healing, enabled by large reconstructive bonding displacements within the open structure.[15,16] Beyond optoelectronic applications, recent efforts are also revisiting the crystalline-amorphous transition of Sb_2Se_3 for phase change based reconfigurable photonic devices.[17–19] This reversible transition in the orthorhombic antimonides is rare in that it maintains near-zero losses in the near- to mid-infrared spectral ranges across both defective polycrystalline and amorphous states.[19] Collectively, these applications underscore the broad impact of this material system, pointing to exciting avenues for future research and technological development.

From both fundamental characterization and device standpoints, the properties of Sb_2Se_3 are made more intriguing by the strong anisotropy of the crystal,[3,20] and as such, merit investigation of synthesis routes that reliably reproduce and realize such anisotropy to harness its full electronic or optical utility. Focusing on applications in photonics, the very low-loss, high-index, and birefringent character of Sb_2Se_3 makes it an ideal candidate for integrated photonics. While prior experimental work on the optical anisotropy of single crystal or bulk Sb_2Se_3 is hard to find, first-principles modeling suggests biaxial character with giant birefringence as high as 0.64 between the 1D axis direction (formed from covalently-bonded Sb and Se atoms) and the primary vdW-bonded direction.[3] This is borne out experimentally in the isostructural bulk Sb_2S_3 crystals with birefringence of ~0.9 at 800 nm.[20] Films of naturally anisotropic materials[21] offer a complement to current approaches that use form-birefringence

achieved by nanostructuring isotropic materials, which is lossy and challenging to fabricate. Single-crystalline or suitably textured Sb_2Se_3 films can offer much needed functionality where birefringence or dichroism is harnessed in integrated components for polarization-sensitive light detection, polarization rotating waveguides, and even higher index contrast in amorphous to single crystalline transitions. As a specific use-case, we note integrated photonics are inherently polarization sensitive, which poses a serious limitation compared to free-space optics. Current efforts in polarization conversion in integrated photonics primarily employ sub-wavelength gratings that inevitably introduce additional loss.[22,23] Therefore, a low-loss anisotropic material integrated on photonic waveguides may help resolve this polarization discrimination.

While dissimilar growth interfaces in heteroepitaxy are energetically unaccommodating, the van der Waals epitaxy growth mode adopted by low-dimensional materials partially relaxes structural and bonding constraints,[24] opening exciting pathways towards integration with conventional single crystal cubic platforms. In this respect, healthy initial progress in heteroepitaxy of layered Bi_2Se_3, Bi_2Te_3, and Sb_2Te_3 on GaAs(001) and Si(111) substrates has been made,[25–29] yet ultra-high vacuum (UHV) film deposition methods for the orthorhombic V-VIs (Sb_2Se_3 and Sb_2S_3) remain underdeveloped. With molecular beam epitaxy (MBE), capabilities to monitor surface preparation and produce controlled growth rates may advance tuning of substrate-film interactions. We note demonstrations of heteroepitaxial growth of Sb_2Se_3 on muscovite mica substrates using vapor transport deposition[30] and on Bi_2Se_3 epilayers via MBE.[31,32] Both reports are encouraging examples of oriented Sb_2Se_3 growth, and they target distinct applications for Sb_2Se_3 in flexible electronics and topological phenomena, respectively. In this study, we aim to address practical challenges involving Sb_2Se_3 films on surfaces not of hexagonal or trigonal arrangement as has been demonstrated, but on technologically prevalent (001)-type cubic surfaces utilized in photonics. Here, we focus on the commercially accessible GaAs(001) substrate with the objective of exploring the Sb_2Se_3 synthesis space through growth temperature, Se and Sb beam fluxes, and substrate symmetry parameters. These constitute an initial investigation of whether Sb_2Se_3 growth is amenable to atomically clean III-V surfaces, and if the film structure can be systematically controlled despite the unorthodox stibnite structure. Sb_2Se_3 growth on conventional substrates may facilitate device integration beyond photonics; more recently, MBE growth of Sb_2Se_3 also on GaAs yielded nanostructures potentially useful for electronic applications.[33]

It is important to state that the Sb_2Se_3 literature has mainly cited two space group conventions (*Pnma* and an equivalent setting *Pbnm*). As evidenced by numerous works

dedicated to characterizing and optimizing the orientation of Sb_2Se_3,[9,13,34–37] explicit and consistent crystallographic indexing of the low symmetry Sb_2Se_3 material is critical to accurate cross-interpretation.[38] To avoid ambiguity, we reiterate that the *Pbnm* convention (a = 11.63 Å, b = 11.78 Å, c = 3.98 Å in the bulk, with [001] covalently-bonded chains) has been adopted for conceptual convenience throughout this work.

2. Results and Discussion

2.1. Nucleation, growth, and morphology

Sb_2Se_3 films were prepared using molecular beam epitaxy (MBE) and separate Sb and Se solid sources. The high vapor pressure of Sb and Se require lower growth temperatures to enable sufficient adsorption and subsequent incorporation into the Sb_2Se_3 compound. With Sb and Se shutters open, we did not observe changes in reflection high energy electron diffraction (RHEED) until the substrate temperature approached ~280 °C and below, suggesting desorption of the impinging Sb and Se at temperatures above 280 °C. We find successful growth temperatures (T_g) for crystalline films were between 180–265 °C. At 150 °C or below, we observe disordered phases of Sb_2Se_3 (**Figure S1** and **Figure S2**). The quality of the crystalline films was found to depend on substrate preparation. The first preparation is termed Se-treated GaAs, an epi-ready wafer which undergoes 600 °C thermal deoxidation under a Se overpressure prior to growth; the second is pristine regrown (homoepitaxial) GaAs preserved under an arsenic cap. This surface cap is also thermally desorbed prior to growth, but at much lower temperatures near 400 °C and without an intentional Se overpressure. We refer the reader to the film synthesis methodology for further details on III-V substrate preparation. Other growth parameters are also summarized for the films in this study in **Table SI**.

Several film morphologies measured by atomic force microscopy (AFM) and corresponding RHEED patterns are compared in **Figure 1**. At substrate temperatures of 265 °C or below, we observe that growth of crystalline Sb_2Se_3 directly on Se-treated GaAs forms a rough microstructure. As shown in Figure 1a, protruding and mixed orientation crystallites are plentiful in the film grown on Se-treated GaAs and compromise the overall film quality. In Figure 1b, the chevron pattern RHEED, typical of a rough 3D growth mode, further supports that a Se-treated surface is suboptimal for nucleation and growth. Over the growth duration, the intensity of RHEED slightly dims, suggesting that film quality struggles to improve even after the interface has been overgrown. Misoriented grains are particularly detrimental for Sb_2Se_3 film morphology because the crystal habits in stibnites may embody prismatic or bladed forms. This is patently clear in an additional film grown at 265 °C with an increased Sb BEP of 2 ×

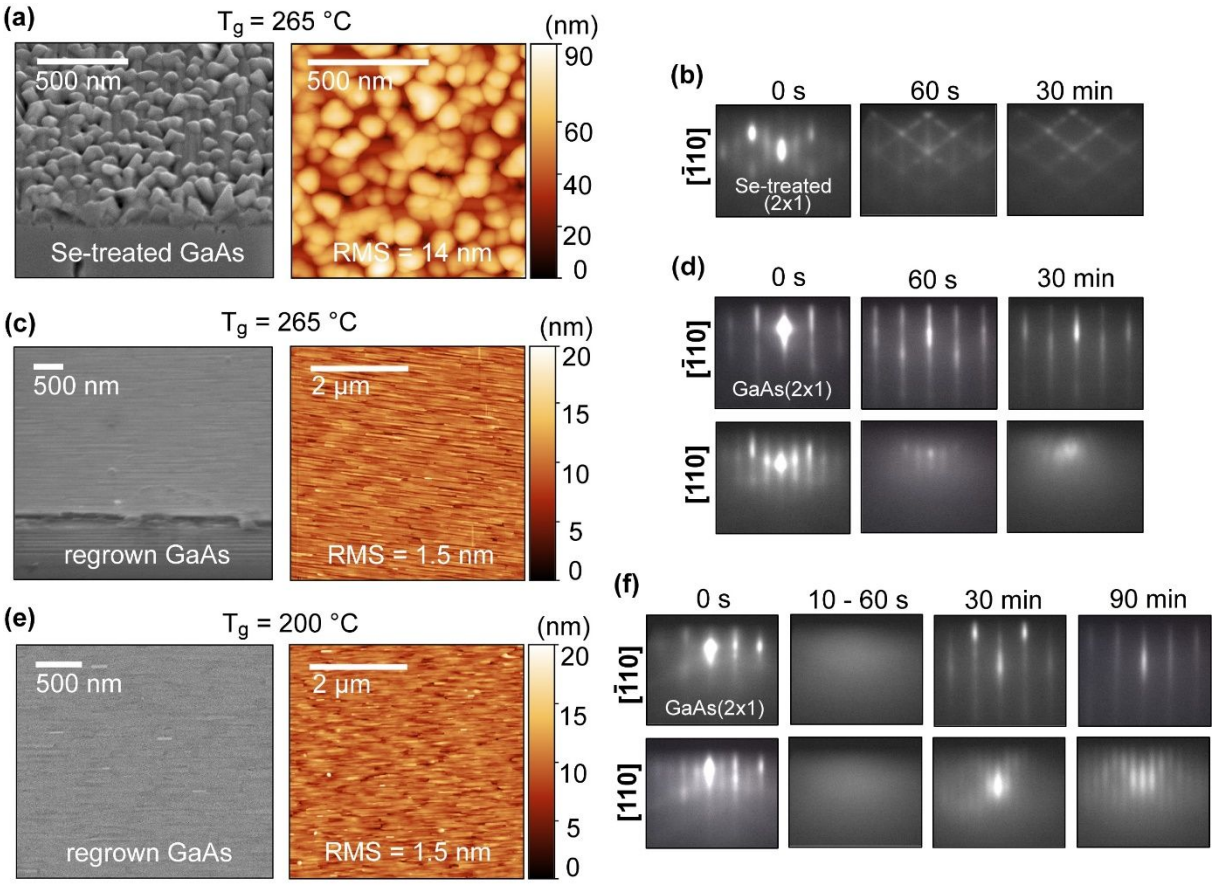

Figure 1. (a) 45°-mounted SEM and AFM, including (b) RHEED pattern of 265 °C Sb_2Se_3 on Se-treated GaAs. (c) 45°-mounted SEM and AFM of 265 °C Sb_2Se_3 film on regrown GaAs, forming a ribbon microstructure. (d) Corresponding RHEED pattern for film in (c), where streakiness appears along GaAs $[\bar{1}10]$ and diffuse streaks develop along [110]. (e) Plan-view SEM and AFM of 200 °C Sb_2Se_3 on regrown GaAs, showing a less well-defined ribbon microstructure. (f) RHEED pattern for an additionally grown 200 °C film of ~3 × thickness. A initial hazy pattern (10–60s) transitions to streaks of different periodicities along GaAs $[\bar{1}10]$ versus [110]. (Note the AFM scan size is 1 × 1 μm² in (a) and 5 × 5 μm² in (c),(e).)

10^{-7} Torr. (This Sb BEP is 4 × greater than the 5 × 10^{-8} Torr BEP otherwise used throughout this work.) These growth conditions promoted inclined shards with poor coalescence across the substrate (**Figure S3**).

The structural quality of the films improves significantly on arsenic-capped regrown GaAs templates. We prepared films under the same growth rate of ~0.4 Å/s on regrown GaAs at T_g = 265 °C and 200 °C. Inclined crystallites are significantly reduced, resulting in an overall smoother and continuous film (Figure 1c and 1e). AFM surface topography indicates an order magnitude of reduction in root mean square (RMS) surface roughness from 14 nm to 1.5 nm by switching to regrown GaAs templates. As captured by SEM and AFM, the primary surface feature of the smoother films is parallel faceting, which creates a distinct ribbon- or rod-like surface structure. At T_g = 200 °C, these parallel structures become less clearly defined, we suspect due to decreased adatom diffusion at the lower growth temperature. Geometric "rod" surface features were also observed for films grown on mica and Bi_2Se_3.[30,32] In these reports,

domains manifested in parallelogram shapes with 60° or 120° angles, as opposed to the 0°/180° or parallel features we observe.

Improved nucleation can also be immediately observed in the RHEED patterns for films synthesized on regrown GaAs (Figure 1d, 1f). Instead of a chevron pattern previously seen in Figure 1b, Sb_2Se_3 RHEED remains streaky throughout the growth period along the GaAs [$\bar{1}$10] direction. Differences emerge in the RHEED pattern following nucleation for these two growth temperatures. At T_g = 265 °C, a faint streaky pattern forms by 60 seconds only along GaAs [110] and further degrades as the film grows thicker. At T_g = 200 °C, upon opening shutters, highly disordered growth first produces a temporary hazy pattern. The hazy pattern lasts across the "10-60 s" frame in Figure 1f. Following the haze, a two-fold streaky pattern along two primary axes of the orthorhombic cell emerges, indicating a transition to longer range order crystalline growth. By the 30 minute mark in Figure 1f, the [110]-aligned streaks are still weak. Extending the growth period, we see by the 90 minute mark that the streak intensity has further increased and shows a clearer periodicity. This likely corresponds with gradual improvement in crystallinity along this second axis in Sb_2Se_3 as the film increases in thickness. We note that different streak periodicities along the [$\bar{1}$10] and [110] azimuths suggest that diffraction arises from real space gratings of shorter and longer periodicity, consistent with the highly dissimilar lattice constants of orthorhombic Sb_2Se_3.

The stark contrast in morphology and RHEED between growths on Se-treated and regrown GaAs suggests that a smoother regrown zincblende surface benefits growth quality significantly. Se-treated GaAs may include defects such as Se-terminated dimer rearrangement or Ga-Se byproducts.[39,40] Additionally, Se-treated GaAs develops surface pits due to the high temperatures required for in-situ oxide removal and related outgassing.[41] Pit formation roughening is quite visible in Figure S3 and degrades the seed quality. Lastly, but perhaps most importantly, Se-treated GaAs does not include a so-called "buffer layer", which is used in traditional III-V MBE to smooth out and restore the surface before subsequent epitaxial material is grown. Sb_2Se_3 appears to be structurally sensitive to surface defects on GaAs(001) and thus all other films discussed in this study are deposited on pristine regrown GaAs templates to preserve smoothness and crystallinity.

2.2 Epitaxial relationship and structural quality

As visually suggested in AFM and SEM, the ribbon surface features of Sb_2Se_3 films are oriented in-plane (IP) to the GaAs substrate, prompting us to investigate the structural properties further

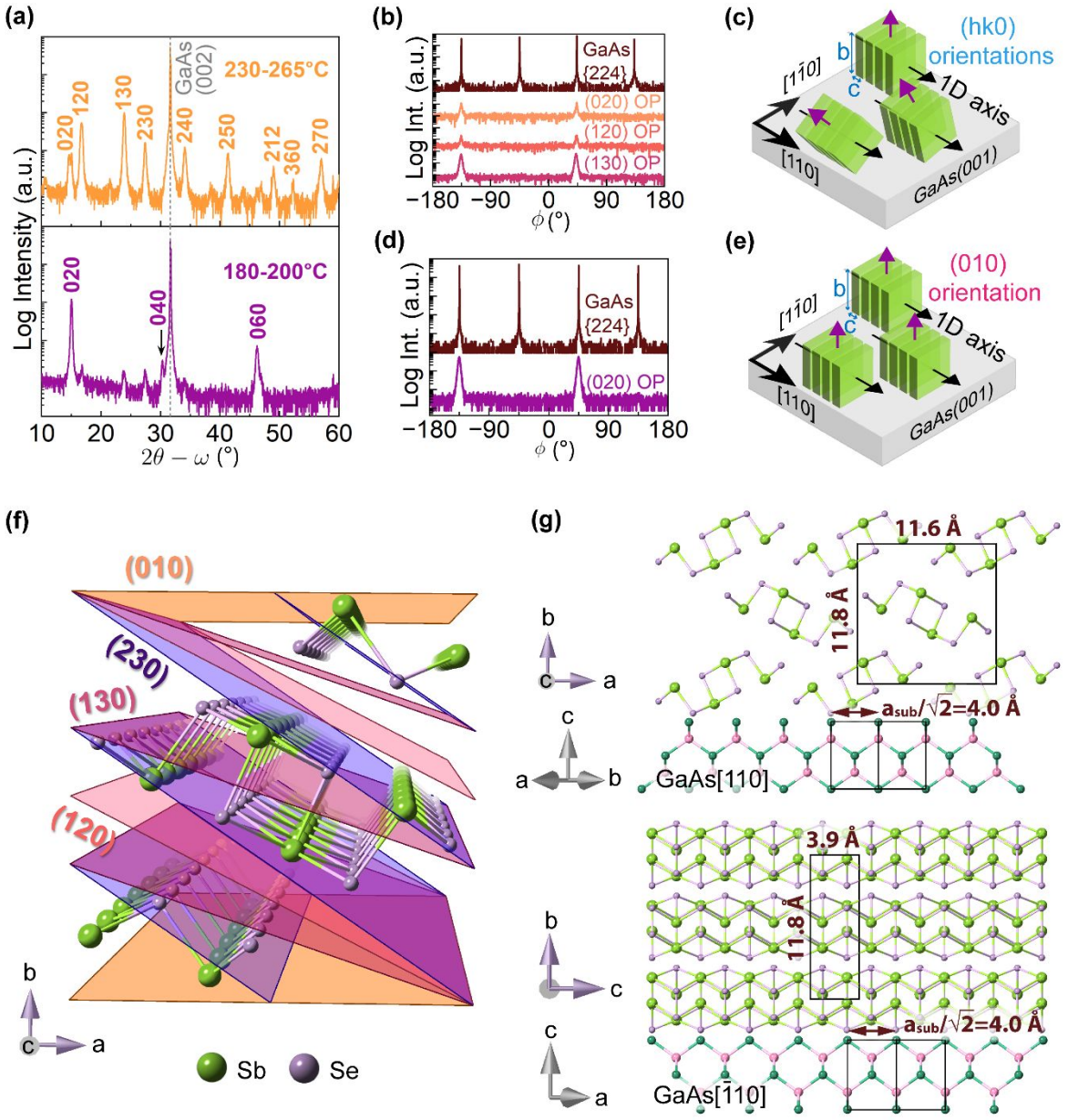

Figure 2. (a) Out-of-plane 2θ-ω scans indicate multiple (hk0) orientations are present in Sb_2Se_3 synthesized between 230–265 °C and a dominant (010)-orientation is present for 180–200 °C. (b) Phi scans of GaAs{224} and asymmetric Sb_2Se_3 reflections for several high volume fraction (hk0)-OP grains in a 230 °C film. The probed Sb_2Se_3 asymmetric planes are (120), (020), and (020)-Sb_2Se_3, respectively corresponding to the three labeled OP orientations of (020), (120), and (130). The Sb_2Se_3 grains show in-plane alignment with GaAs [110]. (c) Schematic diagram of an in-plane textured / (hk0)-oriented film (230–265 °C) showing neighboring grains rotated about their 1D axis. The orthorhombic unit cells are depicted in green. (d) Phi scans of GaAs{224}and the asymmetric Sb_2Se_3-(120) reflection in a 200 °C film. Sb_2Se_3 exhibits in-plane alignment to GaAs [110]. (e) Schematic diagram of an epitaxial (010)-oriented film (180–200 °C). The orthorhombic unit cells are depicted in green. (f) Perspective view illustration of several (hk0) planes within the Sb_2Se_3 unit cell. (hk0) planes are inclined to the horizontal *a*-*c* plane and lie within the [001] zone. (g) Epitaxial orientation of Sb_2Se_3 lattice on GaAs (001) viewed along the in-plane GaAs [110] and [1$\bar{1}$0] directions. Unit cells are outlined in black.

with X-ray diffraction (XRD). We report two types of crystalline structure in two growth temperature regimes of 230–265 °C (in-plane/IP textured) and 180–200 °C (epitaxial). Symmetric out-of-plane (OP) and phi scans, in addition to several structure schematic diagrams, are shown in **Figure 2** to characterize the grain orientations of Sb_2Se_3 on GaAs.

First, we characterize the out-of-plane orientations indicated by 2θ-ω scans in Figure 2a. At higher growth temperatures between 230–265 °C, the film contains mostly mixed (hk0)-oriented OP domains, indicated by the presence of both low- and high-index X-ray reflections in the *Pbnm* space group (upper panel of Figure 2a). Several (hk0) planes are illustrated in Figure 2f. The abundance of both high and low symmetry orientations in Sb_2Se_3 is an unusual observation; we hypothesize that the predominantly vdW character common to (hk0)-plane terminations is responsible for this phenomenon. In general Sb_2Se_3 bonding can be decomposed into two components: (i) intrachain interactions (forming Sb-Se covalent bonds of length 2.59–3.21 Å) and (ii) interchain interactions (vdW-based with longer interatomic distances of 3.24–3.74 Å).[2] Therefore, the (hk0) planes cut through the ribbons at an oblique angle and primarily terminate the weaker interchain interactions within the Sb_2Se_3 unit cell.

Intermediate growth temperatures of 180–200 °C produce films favoring a primary (010)-orientation, as indicated by the first allowed (020) and higher order (040) and (060) reflections in the lower panel of Figure 2a. We believe it is most accurate to categorize this intermediate regime not as entirely independent from the high temperature regime (230–265 °C), but rather as a subtle transition away. Viewed on a logarithmic scale, symmetric 2θ-ω scans reveal that several (hk0) OP orientations present in the T_g = 230 – 265 °C films persist down to 180–200 °C, but their intensities have been dramatically suppressed. This (010)-orientation dominant XRD pattern may point to a more conventional case of vdW materials growth where exposure on a single low energy basal plane is preferred. Several reports have indicated that Sb_2Se_3 may exhibit such hallmarks of 2D vdW systems despite the quasi-1D nature.[3] The weakest bonding exists along one axis in particular, namely [010] which has the furthest atom-to-atom distance in Sb_2Se_3.[2] There are several experimental reports on single crystal Sb_2Se_3 that support this primary (010)-cleavage or (010)-layered behavior.[38,42,43]

As for the in-plane (IP) orientation of Sb_2Se_3, we find the Sb_2Se_3 needle axis (*c*-axis) is aligned to the GaAs [110] directions in both films. This crystallographic alignment is consistent with work by Wojnar *et al*.[33] Phi scans of GaAs {224} and two specific asymmetric planes in Sb_2Se_3 were probed depending on the grain OP orientation. For mixed (hk0)-oriented films, we probed the (120)-plane to understand the IP relationship of the (020) OP grains. Likewise, we used the (020)-plane to understand the orientation of (120) and (130) OP grains. These phi scans are shown in relation to the substrate {224} peaks in Figure 2b. We see that two 180°-separated film peaks share the same azimuth as the GaAs [110] IP directions, indicating the IP relationship, Sb_2Se_3 [001] ∥ GaAs [110], holds for multiple (hk0) OP-oriented grains. An illustrative schematic of these textured films is presented in Figure 2c. In this work, we refer to

these films as IP-textured or (hk0)-oriented Sb_2Se_3. The phi scans also reveal that 180°-rotated twin domains constitute the film. Single crystal orthorhombic Sb_2Se_3 has a single (020) pole; we have instead observed two 180°-separated peaks arising from the asymmetric (020)-plane in Figure 2b.

The 200 °C epitaxial film, with dominant (010) OP grains, is similarly aligned in-plane to GaAs, as evidenced by a phi scan of the asymmetric (120)-Sb_2Se_3 peak (Figure 2d). A schematic of the epitaxial grain structure is depicted in Figure 2e. The epitaxial films are slightly higher crystalline quality than the IP-textured films. Rocking curves (RCs) are large for the IP-textured films, demonstrated by a 1.4° FWHM of the (020) RC and 1.2° FWHM of the (120) RC. The epitaxial films exhibit an out-of-plane (020) RC FWHM = 0.87°, a slight improvement but nonetheless with broadening contributions from low lateral coherence within the film. While these films can be improved structurally, they are distinguished from previous reports of epitaxial Sb_2Se_3 because 90°-rotated orthorhombic domains have been largely suppressed on the cubic substrate—resulting in a fully in-plane anisotropic structure not observed for hexagonally-twinned Sb_2Se_3 grown on more compatible Bi_2Se_3 templates.[32]

Lattice mismatch is a critical parameter that determines the quality of traditional crystalline interfaces and subsequent growth, leading us to consider its potential effects on the orthorhombic-cubic Sb_2Se_3/GaAs interface. The alignment of orthorhombic Sb_2Se_3 (a = 11.63 Å, b = 11.78 Å, c = 3.98 Å) on GaAs (a = 5.65 Å) is depicted in Figure 2g. Epitaxial Sb_2Se_3 crystallizes with the a- and c-axes in-plane, where the highly rectangular a-c face is 45°-rotated with respect to the GaAs (001) face. The a- and c-directions experience different lattice mismatch to the GaAs cubic diagonals. The longer a-axis exhibits a +3% mismatch to GaAs [110], derived from a $d_{SbSe}(100) : 3d_{GaAs}(110)$ ratio where $d_{SbSe}(100)$ = 11.63 Å and $d_{GaAs}(110)$ = 4.00 Å. There exists a smaller and thus more favorable +0.5% lattice mismatch between the shorter c-axis and GaAs [110] ($d_{SbSe}(001) : d_{GaAs}(110)$, where $d_{SbSe}(001)$ = 3.98 Å). However, the role of favorable lattice mismatch in mediating the crystallographic relationship between Sb_2Se_3 [001] and GaAs [110] is unclear. We also observe evidence that substrate symmetry anisotropy plays a large role in influencing the needle direction, as we discuss at the end of this section.

We aim to further understand the transition in growth at the interface for epitaxial films through cross-sectional transmission electron microscopy (XTEM) shown in **Figure 3**. The narrow growth regime in which (010)-oriented epitaxial Sb_2Se_3 forms is identifiable by the evolution of the RHEED pattern from hazy to streaky, shown previously in Figure 1f. High-resolution (HR) or phase-contrast XTEM images in Figure 3a show that Sb_2Se_3 closer to the

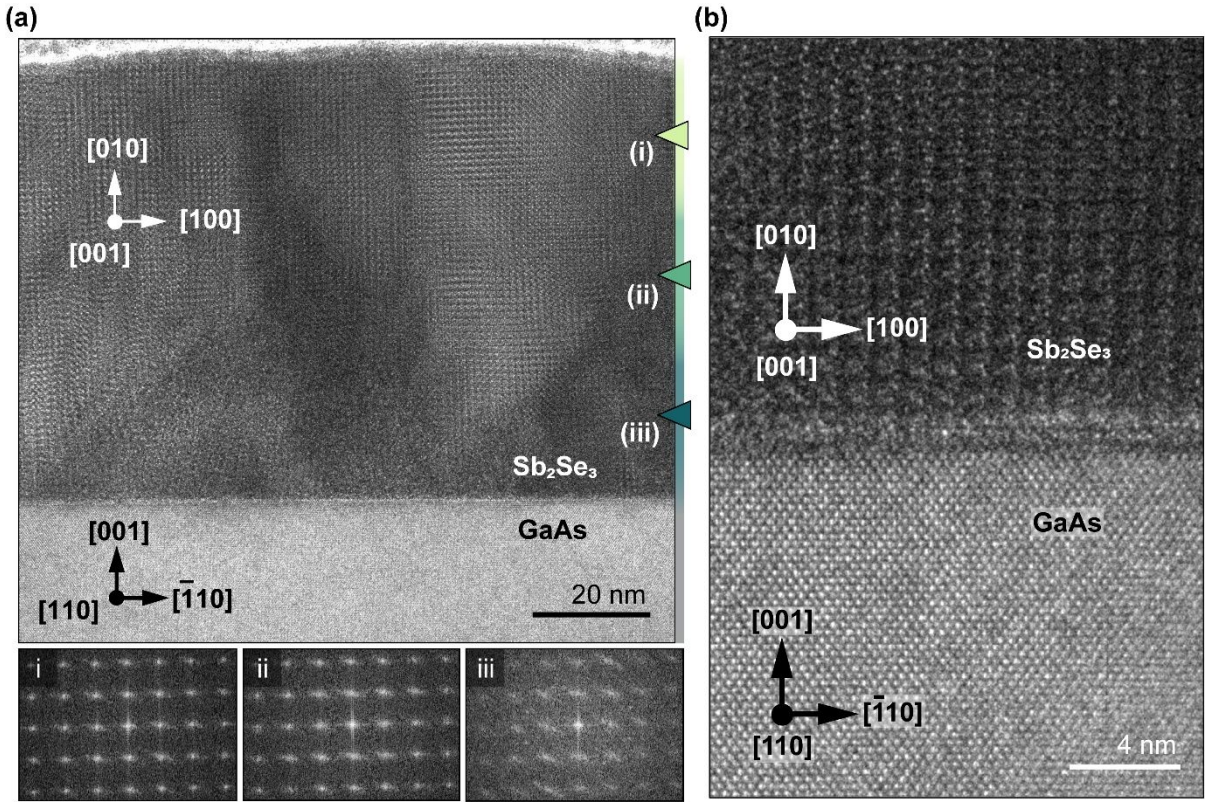

Figure 3. (a) HR-TEM of 76 nm 200 °C Sb_2Se_3 film imaged along the [110] GaAs zone axis. (i)-(iii) FFTs at three lateral regions away from the film-substrate interface. The FFT reciprocal lattice exhibits elongated or arced points in region (iii), which is closest to the interface, and collapses into increasingly sharper points moving away from the interface in regions (ii) and (i). (b) (010)-orientation Sb_2Se_3 grain directly nucleated on GaAs.

interface contains regions of misoriented lattice but is otherwise crystalline. Although hazy RHEED patterns are typically suggestive of amorphous character, in this case, it is possible that the initial growth suffers from such short-range lateral coherency relative to that of the electron beam that coherent diffraction does not occur. RHEED detects coherence on lengths of at least 100 nm.[44,45] We speculate that local clusters which had fortuitously nucleated in the primary vdW (010) orientation were energetically favorable sites for subsequent growth over other grain orientations. An example of such a (010)-oriented region is shown in Figure 3b.

An alternative explanation for a disorder-to-order RHEED transition was proposed by Shayduk and Braun in MBE-grown cubic $Ge_2Sb_2Te_5$ on GaSb(001).[46] They hypothesized that the initial disordered phase crystallized epitaxially after sufficient incubation time to seed further epitaxial growth. This growth mechanism is not active in our experiment. Had the epitaxial seed of Sb_2Se_3 come from a transformed interface layer, we would expect to resolve lattice fringes signaling improved registry between the interface and the rest of the film, without signatures of overgrowth. In Figure 3a(i)-(iii), we find that fast Fourier transforms (FFTs) taken along three lateral regions gradually further from the interface increasingly sharpen, indicating one contributor to improved structural quality is lower misorientation within the film as the (010)-orientation successfully overgrows. Inspecting the XTEM images further away from the

Sb_2Se_3/GaAs interface, we find that some regions of the (010)-Sb_2Se_3 film produce clearer lattice fringes than others. This additionally points to a wide range of in-plane Sb_2Se_3 grain orientations about the GaAs [110] zone axis. The skew-symmetric (120)-Sb_2Se_3 RC exhibits a large FWHM of ~1.5°, further supporting the presence of severe twist distortion in the 200 °C film. These structural characteristics point to the soft bonding of the Sb_2Se_3 crystal and the relatively low growth temperatures used.

The Sb_2Se_3 films otherwise growing epitaxially or with IP parallel domains requires factors which break the high symmetry of the substrate. We find that the (2×1) GaAs surface reconstruction, which likely modulates the interface energy as well as in-plane adatom diffusivity, plays a critical role. We hypothesize anisotropic cation mobility and diffusion across GaAs[47] has promoted the in-plane ordering of Sb_2Se_3. Directions with longer migration lengths would preferentially promote Sb_2Se_3 growth along its *c*-axis, as [001] sites are more active and readily available for adatom incorporation. When (2×1) GaAs was exchanged with a higher symmetry rocksalt (1×1) PbSe(001) template, the film consisted of four 90°-rotated populations instead (**Figure S4**). There is an even greater lattice mismatch of +8.0% between Sb_2Se_3 [001] and PbSe [110], as the PbSe lattice constant is 6.12 Å.

The relative group VI and V fluxes may also modulate diffusivity anisotropy on GaAs. We have demonstrated that under Sb and Se BEPs of 5×10^{-8} Torr and 1×10^{-6} Torr, respectively, that the surface is lightly corrugated from parallel-faceted grains. However, additional films prepared at 200 °C and lower Se BEPs suggest that the film morphology and in-plane needle alignment suffer (**Figure S5**) without sufficient Se overpressure at 1×10^{-6} Torr, highlighting the role of flux tuning to additionally set the epitaxial relationship. This Se BEP is indeed quite large, and we additionally notice that accumulated Se in the chamber negatively impacts the (010) OP orientation upon repeating consecutive 200 °C growths (**Figure S6**). With sufficient time to pump away the volatile Se vapor, we see recovery of epitaxial growth and repeatability of this procedure. Therefore, (i) exploring other low symmetry templates with exaggerated surface anisotropy and (ii) ensuring a low Se environment prior to growth (to preserve a pristine surface) may improve monocrystallinity of Sb_2Se_3 thin films. This potentially has positive implications for UHV growth on CMOS-compatible cubic substrates that also develop a (2×1) reconstruction, such as Si and Ge (001).[48]

2.3 Optical anisotropy

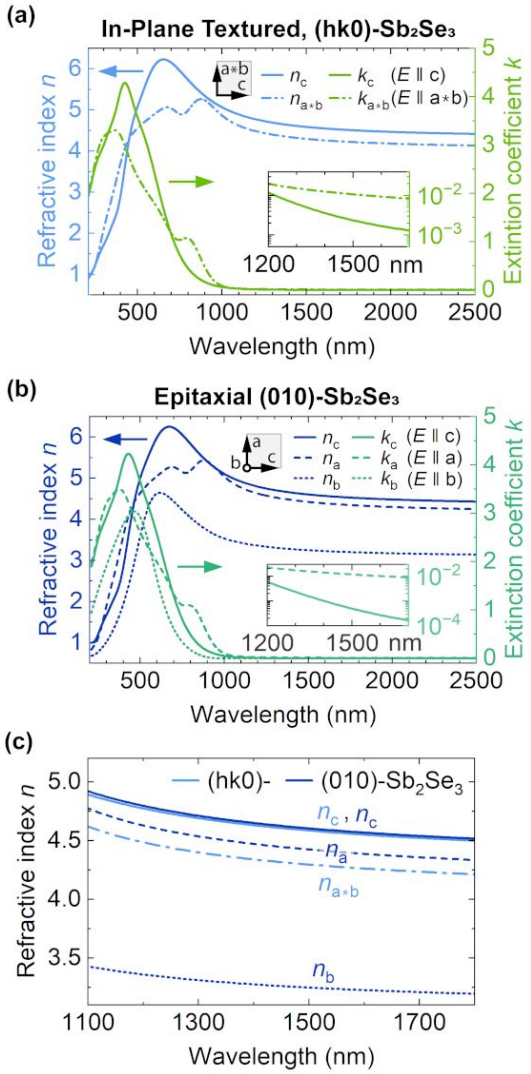

Figure 4. Refractive indices and extinction coefficients (n, k) from 210–2500 nm for (a) in-plane textured / (hk0)-orientation and (b) epitaxial (010)-orientation Sb_2Se_3 film. Insets show the extinction coefficients across 1200–1700 nm on a log scale. (c) Comparison of the n_c, n_{a*b} refractive indices in (hk0)-oriented Sb_2Se_3 versus n_c, n_a, and n_b in (010)-Sb_2Se_3 from 1100 to 1800 nm. The in-plane indices are n_c, n_a and the out-of-plane index is n_b for (010)-Sb_2Se_3.

The relationship between the structure and optical properties in the Sb_2Se_3 films are highlighted in this section. Orthorhombic crystals are optically biaxial, an intriguing property which fundamentally originates from anisotropic atomic arrangements and their differences in polarizability. Conventional layered materials, with strong covalent bonding within layers and weak vdW bonding between layers, exhibit strong out-of-plane birefringence.[49,50] In orthorhombic layered materials, the refractive properties are different along all three crystal axes, uniquely enabling both out-of-plane and in-plane anisotropy. The films in this study preserve structural anisotropy and may serve as a platform to investigate the expectedly biaxial properties of Sb_2Se_3.

The film anisotropy is indeed reflected in the non-zero Mueller matrix off-diagonal terms (**Figure S7** and **Figure S8**). The complex refractive index (n + ik) across 210–2500 nm

obtained from generalized ellipsometry for the IP-textured and epitaxial (010)-Sb_2Se_3 films are shown in **Figure 4**. We present the in-plane *n* and *k* optical constants of the films approximately along the distinct GaAs [110] and [$\bar{1}$10] directions. Additionally, for epitaxial Sb_2Se_3, the out-of-plane index is presented to look for giant birefringence.

Figure 4a shows the in-plane indices for the IP-textured Sb_2Se_3 film. The first set of constants along GaAs [110] (n_c, k_c) corresponds to polarization along the Sb_2Se_3 *c*-axis, and the second set of constants along GaAs [$\bar{1}$10] (n_{a*b}, k_{a*b}) corresponds to polarization along the Sb_2Se_3 *a*- and *b*-directions. (The a ∗ b subscript denotes weighted average contributions from *a*- and *b*- because of the rotated Sb_2Se_3 grains about their *c*-axis, as depicted previously in Figure 2c.)

Figure 4b shows the full indices for epitaxial (010)-Sb_2Se_3. Here, the first set of constants are also n_c, k_c. However, the second set of constants corresponds to polarization primarily along the *a*-axis (n_a, k_a). The final third set of constants corresponds to polarization in the out-of-plane direction or primarily along the *b*-axis (n_b, k_b). We caution the reader against ascribing certainty to n_b and k_b in the absorbing region approaching the visible and UV wavelengths. We note that reflection-mode ellipsometry loses sensitivity to out-of-plane orientation when the refracted p-polarization is strongly absorbed in the film, therefore leaving s-polarization, which probes only the in-plane properties.[51] Also, the out-of-plane absorption towards the near-infrared range is assumed to be zero (k_b = 0) in our model. We make this assumption based on other experimental reports suggesting Sb_2Se_3 absorbs minimally below its bandgap.[6,19] In the transparent region, the out-of-plane refractive index fit can be reported with greater confidence.

We compare the indices between IP-textured and epitaxial films more closely in Figure 4c. Looking at the transparent C-band telecom wavelength (λ = 1550 nm), IP-textured (hk0)-Sb_2Se_3 exhibits in-plane indices of n_c = 4.57 and n_{a*b} = 4.28, with a remarkable in-plane birefringence of 0.29 (Figure 4a). We have not measured the out-of-plane index. Epitaxial (010)-Sb_2Se_3 exhibits n_c = 4.59, n_a = 4.41, and n_b < 3.5—a giant birefringence exceeding 1 in the *b*-*c* plane that is among the largest values reported for an epitaxially integrated thin film in the near-infrared. This hierarchy of optical properties arises from its underlying bonding—the needle direction exhibits the highest refractive index (*Pnma*: n_b, *Pbnm*: n_c), ribbon sheet direction second (*Pnma*: n_c, *Pbnm*: n_a), and primary vdW direction lowest (*Pnma*: n_a, *Pbnm*: n_b), in agreement with studies on single crystal Sb_2S_3 (reported in Schubert *et al.* under the *Pnma* convention).[20] This hierarchy in the orthorhombic Sb_2X_3 crystals reflects the refractive indices at sub-bandgap wavelengths tending to be highest along the covalently-bonded direction

relative to more weakly-bonded directions. Here, the lowest index is indeed along the *b*-axis (*Pbnm* convention) which bears the greatest van der Waals character.

In Figure 4c, we note the n_c indices are comparable across these samples as expected, suggesting refractive properties are similar in both IP-textured and epitaxial structures for polarization maintained parallel to the needle direction. This considerably expands the temperature growth window for Sb_2Se_3 on GaAs for photonic applications from epitaxial films to also include the IP-textured films. We also observe that n_{a*b} of the IP-textured film is lower than n_a. This is due to the index along the primary vdW direction (n_b) being lowest in the hierarchy and decreasing the weighted n_{a*b} index, yielding enhanced IP-anisotropy in these samples compared to the epitaxial films. The in-plane and out-of-plane birefringence at the O-band (λ = 1310 nm) is similar in value to that at 1550 nm.

Furthermore, near-infrared attenuation is found to be low in these films (Figures 4a-b), as the extinction coefficients k are on the order of 10^{-2} and below when the polarization lies within the plane of the film. The confluence of birefringence and high transmission in Sb_2Se_3 in the near-infrared may be beneficial in devices that require polarization tuning or phase control. Towards the visible range, the in-plane extinction coefficients k_c vs. k_{a*b}/k_a are no longer so similar and become of notable magnitude, suggesting dichroism could be an additional functionality for shorter wavelengths, especially around 600–1000 nm.

3. Conclusion

We have developed thin films of orthorhombic Sb_2Se_3 on cubic GaAs(001) using molecular beam epitaxy. Structurally, these films exhibit preferred alignment of the Sb_2Se_3 1D axis to GaAs [110] at low growth temperatures of 180–265 °C. We demonstrate that these films are low-loss and are optically biaxial. They preserve out-of-plane and in-plane optical anisotropy with giant birefringence approaching 1 at telecom bands, and uniquely also an in-plane anisotropy along orthogonal directions approaching 0.3. Our work marks a development towards fully anisotropic Sb_2Se_3 films synthesized on technologically relevant cubic templates, a significant departure from previous reports achieving three or six rotational domains that yield in-plane isotropic behavior. We anticipate two important avenues for further study in electronics and photonics. Improvement in the mosaicity and in-plane twist in the epitaxial films will lead to application in a range of minority carrier devices, while transfer of the growth principles derived from our work on GaAs to CMOS-compatible substrates such as Si and Ge would further facilitate integration of Sb_2Se_3 and bring exciting orientation-dependent functionalities to existing photonic schemes.

4. Experimental

***Sb_2Se_3 Thin Film Synthesis*:** A Riber Compact 21 (C21) chalcogenide MBE equipped with elemental valved Sb and Se cracker sources was used to grow Sb_2Se_3 thin films of thicknesses 72–228 nm on single crystal GaAs(001) substrates. Growth temperatures were read from an optical pyrometer. The beam equivalent pressures (BEPs) of the Sb and Se sources were maintained at 5×10^{-8} Torr and 1×10^{-6} Torr, respectively, for a growth rate of ~0.4 Å/s. Film growth rates were determined using thicknesses values obtained from X-ray reflectivity measurements (XRR).

To prepare pristine homoepitaxial GaAs(001) templates prior to Sb_2Se_3 growth, commercial epi-ready GaAs wafers were first loaded into a separate Veeco Gen III MBE. The surface oxide was removed by thermal desorption at 600 °C, followed by growth of ~100 nm homoepitaxial GaAs under an arsenic overpressure. The homoepitaxial GaAs templates were then capped in-situ with an amorphous arsenic layer. These capped homoepitaxial substrates were taken out-of-vacuum, cleaved into 1×1 cm^2 sections, and indium-bonded to molybdenum platens. For cold growths below 150°C, cleaved quarter-wafer pieces were secured to a separate molybdenum sample holder designed for indium-free mounting. (An indium-free mount avoids heating effects that would have otherwise been introduced in the indium-debonding process following growth.)

The substrates were subsequently introduced into the Riber C21 chamber, where the amorphous arsenic cap was thermally desorbed and the regrown GaAs template was held to stabilize a (2×4) reconstruction. Residual chalcogenide fluxes from beam pressure calibrations or preceding growths within a single day commonly resulted in an immediate conversion to a (2×1) surface, as indicated by RHEED. After stabilization of the GaAs surface reconstruction, Sb and Se source shutters were opened to initiate film growth at Sb_2Se_3 growth temperatures.

A Se-treated GaAs surface preparation in the C21 MBE is also presented for comparison, in which the substrate native oxide is thermally desorbed under a Se overpressure of 2×10^{-7} Torr prior to initiating growth. The Se flux is supplied due to the absence of an As source in the C21 MBE.

***Structural Characterization*:** Film structure was characterized with scanning electron microscopy (SEM), atomic force microscopy (AFM), X-ray diffraction (XRD), and

transmission electron microscopy (TEM). Standard plan-view and 45°-mounted scanning electron micrographs of films were acquired using a ThermoFisher Apreo SEM (5 kV, 50 pA) and JEOL JSM-IT500HR SEM (10 kV). In the TF Apreo instrument, the electron signal was collected using in-lens detectors. Surface topographical features were analyzed with a Park NX-10 AFM in tapping mode and a NCS15 probe. XRD scans were acquired on a PANanalytical X'Pert Pro MRD instrument with mirror and parallel-plate collimator optics and Ni-filtered Cu-Kα radiation. Cross-sectional lamella of Sb_2Se_3 films were milled in a FEI Helios NanoLab 600i DualBeam. High resolution TEM (HR-TEM) imaging was conducted using a FEI Titan E-TEM (300 kV) and images recorded on a Gatan OneView camera.

***Optical Characterization*:** Variable angle reflection-mode Mueller matrix ellipsometry measurements between wavelengths of 210–2500 nm were acquired on a J.A. Woollam RC2. To ascertain the anisotropy of the crystalline thin films, three datasets were recorded at multiple azimuthal orientations: the samples were rotated in-plane 0°, 45°, and 90° counterclockwise relative to the Sb_2Se_3 1D axis. The three datasets collected at multiple incidence angles between 55°–75° were used to fit the complex anisotropic refractive index within J.A. Woollam's CompleteEASE analysis software. For crystalline-Sb_2Se_3, multiple Gaussian oscillators were employed for fitting of in-plane optical constants. For epitaxial films, films of separate thicknesses were used to help fit the out-of-plane index under a separate Tauc-Lorentz model.

Conflicts of Interest

There are no conflicts to declare.

Supporting Information

The data supporting this article have been included as part of the Supplementary Information.

Acknowledgements

The authors thank N. Hong from J.A. Woollam for helpful discussions on ellipsometry measurements and fitting. We gratefully acknowledge support for materials synthesis and structural characterization via the NSF CAREER Award under Grant No. DMR-2036520. Part of this work was performed at the Stanford Nanofabrication Facilities (SNF) and Stanford Nano Shared Facilities (SNSF), supported by the National Science Foundation under award ECCS-2026822. A. M., V. T., and R. C. are supported by the DARPA-ATOM program. J. E. M.

gratefully acknowledges support from the Tomkat Center for Sustainable Energy's Tomkat Center Graduate Fellow for Translational Research Fellowship.

References

1 G. P. Voutsas, A. G. Papazoglou, P. J. Rentzeperis and D. Siapkas, *Z. Kristallogr. - Cryst. Mater.*, 1985, **171**, 261–268.
2 N. W. Tideswell, F. H. Kruse and J. D. McCullough, *Acta Cryst*, 1957, **10**, 99–102.
3 X. Wang, Z. Li, S. R. Kavanagh, A. M. Ganose and A. Walsh, *Phys. Chem. Chem. Phys.*, 2022, **24**, 7195–7202.
4 C. Chen, D. C. Bobela, Y. Yang, S. Lu, K. Zeng, C. Ge, B. Yang, L. Gao, Y. Zhao, M. C. Beard and J. Tang, *Front. Optoelectron.*, 2017, **10**, 18–30.
5 L. R. Gilbert, B. Van Pelt and C. Wood, *J. Phys. Chem. Solids*, 1974, **35**, 1629–1632.
6 C. Wood, Z. Hurych and J. C. Shaffer, *J. Non-Cryst. Solids*, 1972, **8–10**, 209–214.
7 W. M. Yim, E. V. Fitzke and F. D. Rosi, *J Mater Sci*, 1966, **1**, 52–65.
8 H. L. Uphoff and J. H. Healy, *J. Appl. Phys.*, 1963, **34**, 390–395.
9 X. Wen, C. Chen, S. Lu, K. Li, R. Kondrotas, Y. Zhao, W. Chen, L. Gao, C. Wang, J. Zhang, G. Niu and J. Tang, *Nat Commun*, 2018, **9**, 2179.
10 C. Chen, L. Wang, L. Gao, D. Nam, D. Li, K. Li, Y. Zhao, C. Ge, H. Cheong, H. Liu, H. Song and J. Tang, *ACS Energy Lett.*, 2017, **2**, 2125–2132.
11 Y. C. Choi, T. N. Mandal, W. S. Yang, Y. H. Lee, S. H. Im, J. H. Noh and S. I. Seok, *Angew. Chem. Int. Ed.*, 2014, **53**, 1329–1333.
12 M. Leng, M. Luo, C. Chen, S. Qin, J. Chen, J. Zhong and J. Tang, *Appl. Phys. Lett.*, 2014, **105**, 083905.
13 Z. Li, X. Liang, G. Li, H. Liu, H. Zhang, J. Guo, J. Chen, K. Shen, X. San, W. Yu, R. E. I. Schropp and Y. Mai, *Nat. Commun.*, 2019, **10**, 125.
14 G.-X. Liang, Y.-D. Luo, S. Chen, R. Tang, Z.-H. Zheng, X.-J. Li, X.-S. Liu, Y.-K. Liu, Y.-F. Li, X.-Y. Chen, Z.-H. Su, X.-H. Zhang, H.-L. Ma and P. Fan, *Nano Energy*, 2020, **73**, 104806.
15 I. Mosquera-Lois, S. R. Kavanagh, A. Walsh and D. O. Scanlon, *npj Comput. Mater.*, 2023, **9**, 25.
16 K. P. McKenna, *Adv. Electron. Mater.*, 2021, **7**, 2000908.
17 M. Delaney, I. Zeimpekis, D. Lawson, D. W. Hewak and O. L. Muskens, *Adv. Funct. Mater.*, 2020, **30**, 2002447.
18 D. Lawson, D. W. Hewak, O. L. Muskens and I. Zeimpekis, *J. Opt.*, 2022, **24**, 064013.
19 K. Aryana, H. J. Kim, Md. R. Islam, N. Hong, C.-C. Popescu, S. Makarem, T. Gu, J. Hu and P. E. Hopkins, *Opt. Mater. Express*, 2023, **13**, 3277.
20 M. Schubert, T. Hofmann, C. M. Herzinger and W. Dollase, *Thin Solid Films*, 2004, **455–456**, 619–623.
21 S. Niu, G. Joe, H. Zhao, Y. Zhou, T. Orvis, H. Huyan, J. Salman, K. Mahalingam, B. Urwin, J. Wu, Y. Liu, T. E. Tiwald, S. B. Cronin, B. M. Howe, M. Mecklenburg, R. Haiges, D. J. Singh, H. Wang, M. A. Kats and J. Ravichandran, *Nat. Photon.*, 2018, **12**, 392–396.
22 F. Zhang, J. Zheng, Y. Song, W. Liu, P. Xu and A. Majumdar, *OSA Contin.*, 2020, **3**, 560.
23 H. Jin, L. Niu, J. Zheng, P. Xu and A. Majumdar, *Opt. Express*, 2023, **31**, 10684.
24 A. Koma, *Thin Solid Films*, 1992, **216**, 72–76.
25 X. Liu, D. J. Smith, H. Cao, Y. P. Chen, J. Fan, Y.-H. Zhang, R. E. Pimpinella, M. Dobrowolska and J. K. Furdyna, *J. Vac. Sci. Technol. B.*, 2012, **30**, 02B103.

26 Z. Zeng, T. A. Morgan, D. Fan, C. Li, Y. Hirono, X. Hu, Y. Zhao, J. S. Lee, J. Wang, Z. M. Wang, S. Yu, M. E. Hawkridge, M. Benamara and G. J. Salamo, *AIP Adv.*, 2013, **3**, 072112.

27 X. Liu, Y. P. Chen, D. J. Smith, Y.-H. Zhang, C. Liu, M. Z. Hasan, M. Dobrowolska, J. K. Furdyna, J. Fan, H. Cao, T.-L. Wu and R. E. Pimpinella, in *Bismuth-Containing Compounds*, eds. H. Li and Z. M. Wang, Springer New York, New York, NY, 2013, vol. 186, pp. 263–279.

28 Z. Wang and S. Law, *Cryst. Growth Des.*, 2021, **21**, 6752–6765.

29 J. Momand, J. E. Boschker, R. Wang, R. Calarco and B. J. Kooi, *CrystEngComm*, 2018, **20**, 340–347.

30 X. Wen, Z. Lu, L. Valdman, G.-C. Wang, M. Washington and T.-M. Lu, *ACS Appl. Mater. Interfaces*, 2020, **12**, 35222–35231.

31 A. V. Matetskiy, V. V. Mararov, I. A. Kibirev, A. V. Zotov and A. A. Saranin, *J. Condens. Matter Phys.*, 2020, **32**, 165001.

32 Y.-J. Chen, Y.-C. Jhong, P.-Y. Chuang, C.-W. Chong, J.-C.-A. Huang, V. Marchenkov and H.-C. Han, *Chin. J. Phys.*, 2019, **62**, 65–71.

33 P. Wojnar, S. Chusnutdinow, A. Kaleta, M. Aleszkiewicz, S. Kret, J. Z. Domagala, P. Ciepielewski, R. Yatskiv, S. Tiagulskyi, J. Suffczyński, A. Suchocki and T. Wojtowicz, *Nanoscale*, 2024, **16**, 19477–19484.

34 S.-W. Jung, S.-M. Yoon, I.-K. You, B.-G. Yu and K.-W. Koo, . *Nanosci. Nanotechnol.*, 2011, **11**, 1569–1572.

35 X. Wen, Z. Lu, B. Li, G.-C. Wang, M. A. Washington, Q. Zhao and T.-M. Lu, *J. Chem. Eng.*, 2023, **462**, 142026.

36 J. Otavio Mendes, A. Merenda, K. Wilson, A. Fraser Lee, E. Della Gaspera and J. Van Embden, *Small*, 2023, 2302721.

37 R. Kondrotas, J. Zhang, C. Wang and J. Tang, *Sol. Energy Mater. Sol. Cells*, 2019, **199**, 16–23.

38 T. D. C. Hobson and K. Durose, *Mater. Sci. Semicond. Process.*, 2021, **127**, 105691.

39 H. Abe, K. Ueno, K. S. Koichiro Saiki and A. K. Atsushi Koma, *Jpn. J. Appl. Phys.*, 1993, **32**, L1444.

40 H. Cheng, J. M. DePuydt, M. A. Haase and J. E. Potts, *J. Vac. Sci. Technol. B.*, 2018, **8**, 181–186.

41 A. Guillén-Cervantes, Z. Rivera-Alvarez, M. López-López, E. López-Luna and I. Hernández-Calderón, *Thin Solid Films*, 2000, **373**, 159–163.

42 N. Fleck, T. D. C. Hobson, C. N. Savory, J. Buckeridge, T. D. Veal, M. R. Correia, D. O. Scanlon, K. Durose and F. Jäckel, *J. Mater. Chem. A*, 2020, **8**, 8337–8344.

43 T. D. C. Hobson, O. S. Hutter, M. Birkett, T. D. Veal and K. Durose, in *2018 IEEE 7th World Conference on Photovoltaic Energy Conversion (WCPEC) (A Joint Conference of 45th IEEE PVSC, 28th PVSEC & 34th EU PVSEC)*, IEEE, Waikoloa Village, HI, 2018, pp. 0818–0822.

44 L. Däweritz, in *Handbook of Surfaces and Interfaces of Materials*, 2001, pp. 351–386.

45 A. Ohtake, *Surf. Sci. Rep.*, 2008, **63**, 295–327.

46 R. Shayduk and W. Braun, *J. Cryst. Growth*, 2009, **311**, 2215–2219.

47 Y. Watanabe, T. Scimeca, F. M. Fumihiko Maeda and M. O. Masaharu Oshima, *Jpn. J. Appl. Phys.*, 1994, **33**, 698.

48 R. J. Hamers, R. M. Tromp and J. E. Demuth, *Phys. Rev. B*, 1986, **34**, 5343–5357.

49 G. A. Ermolaev, D. V. Grudinin, Y. V. Stebunov, K. V. Voronin, V. G. Kravets, J. Duan, A. B. Mazitov, G. I. Tselikov, A. Bylinkin, D. I. Yakubovsky, S. M. Novikov, D. G. Baranov, A. Y. Nikitin, I. A. Kruglov, T. Shegai, P. Alonso-González, A. N. Grigorenko, A. V. Arsenin, K. S. Novoselov and V. S. Volkov, *Nat Commun*, 2021, **12**, 854.

50 A. Segura, L. Artús, R. Cuscó, T. Taniguchi, G. Cassabois and B. Gil, *Phys. Rev. Materials*, 2018, **2**, 024001.
51 N. Hong, R. A. Synowicki and J. N. Hilfiker, *Appl. Surf. Sci.*, 2017, **421**, 518–528.

Data Availability Statement

The data supporting this article have been included as part of the Supplementary Information.